FULL PAPER

Superparamagnetic Nanostructures for Off-Resonance Magnetic Resonance Spectroscopic Imaging

Eugene Shi Guang Choo, Erwin Peng, Reshmi Rajendran, Prashant Chandrasekharan, Chang-Tong Yang, Jun Ding, Kai-Hsiang Chuang, and Junmin Xue**

This study proposes a new method to generate positive contrast in magnetic resonance imaging (MRI) using superparamagnetic contrast agents. Superparamagnetic nanostructures consisting of octahedron manganese ferrite nanoparticles embedded in spherical nanogels are fabricated using a bottom-up approach. The composite nanoparticles are strongly magnetized in an external magnetic field and produce a unique NMR frequency shift in water protons, which can be demonstrated in MR spectroscopy and imaging to be different from the bulk pool. Moreover, the particles exhibit excellent colloidal stability in aqueous media and good cell biocompatibility. Hence, these particles are potentially useful as biomarkers by taking advantage of the positive contrast effects produced in MRI.

1. Introduction

Magnetic resonance imaging (MRI) is an important diagnostic technique because it has the capability to obtain in vivo tomographic images of living specimens.[1,2] Advantages of MRI as an imaging tool include being non-invasive, non-ionizing, and being able to provide high spatial resolution and penetration depth for detailed internal cross-sectional images of living organisms. Therefore, MRI is arguably the most important imaging tool in clinical diagnostics today that provides anatomical images of internal soft tissues. However, MRI generally lacks sensitivity and specificity in differentiating similar tissue types, which makes it reliant on contrast agents to acquire useful images.[3,4] Two classes of MRI contrast agents based on changing T_1 and T_2 relaxation, are commonly employed. For T_1 contrast agents, paramagnetic metal complexes such as Gd-chelates have been used routinely in clinics.[5] In an applied magnetic field, the paramagnetic ions create magnetic fields of their own, which fluctuate in time, resulting in faster relaxation of nearby water molecules after each radio-frequency excitation. This produces an increased signal that results in bright spots in contrast with the dark background. T_2 contrast agents are generally based on superparamagnetic nanoparticles.[6–8] Superparamangetic nanoparticles generate static but spatially varying magnetic fields that rapidly dephase the spins of water protons. This process reduces the signal and results in dark spots against a bright background. Thus, it can be understood that typical T_1- and T_2-weighted MR images are dependent solely on darkening or brightening effects. The fundamental problem with this approach is that the effects of the contrast agents are often obscured due to the interference of background tissue signal, pathology (such as hemorrhage or edema) and imaging artifacts, particularly those at tissue interfaces.

In recent years, a great deal of research has been focused on other novel contrast agents such as chemical exchange saturation transfer (CEST) agents,[9,10] and heteronuclear contrast agents that contain elements such as ^{19}F, ^{13}C and ^{31}P.[11,12] These contrast agents produce NMR signals that are different from water protons, which effectively eliminate background influence. More recently, Zabow et al. reported a new form of particulate contrast agent based on micromachined double-disk[13] and cylindrical structures.[14] These contrast agents were purposely designed to disrupt magnetic fields at the microscopic level by creating microscopic localized regions of homogeneous magnetic fields that were distinct from that of the environments. Unlike typical MRI contrast agents that only generate image contrast by shortening the T_1 or T_2 relaxation times, these new contrast agents work by shifting the resonant Larmor precession frequencies. Shifts in the ^1H resonance frequency of water was shown to be the result of geometric effects of the magnetic microstructures instead of chemical effects. Such a frequency shift could be exploited for off-resonance MR spectroscopy imaging without the interference of background water. However, microstructured magnetic particles are not suitable for application in living cells or organisms because of its large size and biocompatibility. Current micromachining (top-down) methods do not yet have the capability to scale the

E. S. G. Choo, E. Peng, Prof. J. Ding, Dr. J. M. Xue
Department of Materials Science & Engineering
Faculty of Engineering
National University of Singapore
7 Engineering Drive 1, 117574, Singapore
E-mail: msexuejm@nus.edu.sg
Dr. R. Rajendran, Dr. P. Chandrasekharan, Dr. C.-T. Yang, Dr. K.-H. Chuang
Singapore Bioimaging Consortium
Agency for Science
Technology and Research
11 Biopolis Way, #02-02, 138667, Singapore
E-mail: chuang_kai_hsiang@sbic.a-star.edu.sg

DOI: 10.1002/adfm.201200275

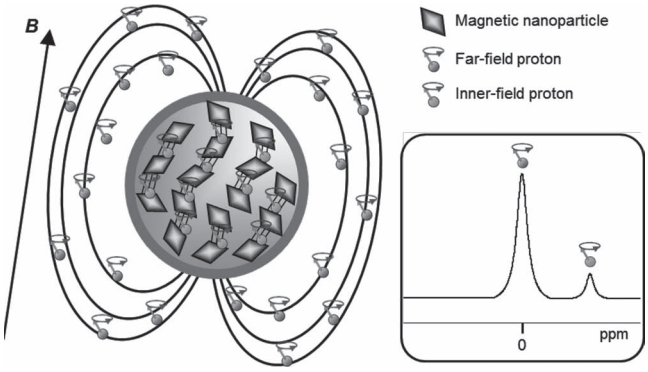

Scheme 1. Schematic diagram depicting the location of water protons in the far-field and inner-field regions of the magnetic nanocomposite. Particles and magnetic flux lines are not drawn to scale. Inset (bottom-right): Specific frequency shift induced upon inner-field protons.

particles down to the nanometer size range while maintaining the high precision. Therefore, we could instead look into chemical synthesis (bottom-up) routes as an alternative to the formation of nanosized magnetic structures for off-resonance MR spectroscopy imaging.

Geometric confinement of magnetic contrast agents in nanoconstructs has shown interesting prospects in improving water relaxivities for both T_1[15] and T_2[16] effects. Hence, magnetic nanostructures are attractive tools for manipulating the magnetic relaxivities. Herein, we attempt to emulate the work of Zabow et al. by using a bottom-up approach to construct a magnetic nanocomposite material composed of magnetic nanoparticles embedded in an amphiphilic copolymer. As illustrated in **Scheme 1**, manganese ferrite nanoparticles (MFNs) with high magnetic moments and highly-faceted octahedron morphology were used as the magnetic components. Using the amphiphilic copolymer as the binding matrix, the MFNs were embedded within spherical nanogels using a previously established miniemulsion method[16] to form manganese ferrite nanocomposite (MFNC) spheres. The MFNs are confined in the polymeric matrix, wherein a proportion of the MFNs may be positioned such that their faceted surfaces (i.e., {111} planes) are aligned. In this way, localized regions of homogeneous magnetic fields that are distinct in magnitude from the surrounding fields could be generated. The spherical nanogels are amphiphilic in nature and allow for the diffusion of water molecules into the spheres. Hence, water protons within the MFNCs could experience a unique NMR frequency shift that is distinct from the bulk environment as shown in the inset of Scheme 1. This offset resonance peak could be exploited for producing a signal that is distinct from water. This has the advantage of eliminating background interference and can be used in conjunction with conventional T_2-weighted imaging to achieve dual-contrast enhancement effects.[17] Of greater significance is that the MFNCs could be well-dispersed in aqueous media with excellent colloidal stability due to their amphiphilic nature, making it potentially useful for in vivo biological applications. Moreover, the nanogels hold excess anhydride rings, which is useful in future work for conjugation with biological probes to incorporate cellular targeting and therapeutic effects.

2. Results and Discussion

2.1. Formation of Magnetic Nanocomposites

As illustrated in **Figure 1**, manganese ferrite nanoparticles (MFNs) were synthesized using $Mn(acac)_2$ and $Fe(acac)_3$ as

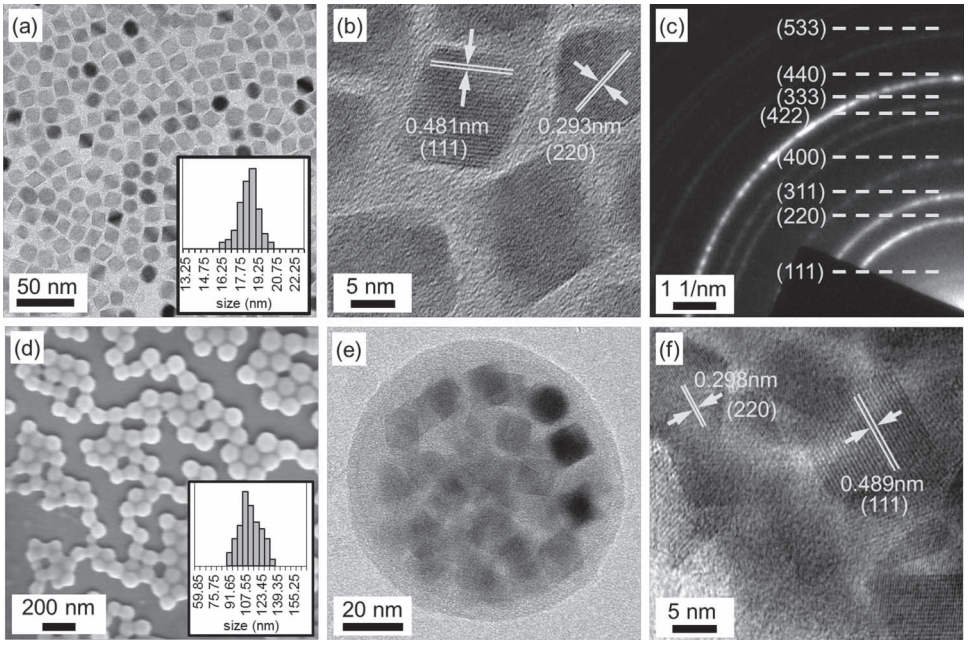

Figure 1. a) TEM image of MFNs (inset: size distribution profile of MFNs); b) high resolution TEM image of MFNs; c) SAED pattern of MFNs; d) SEM image of MFNs; e) TEM image of an MFNC; and f) high resolution TEM of an MFNC.

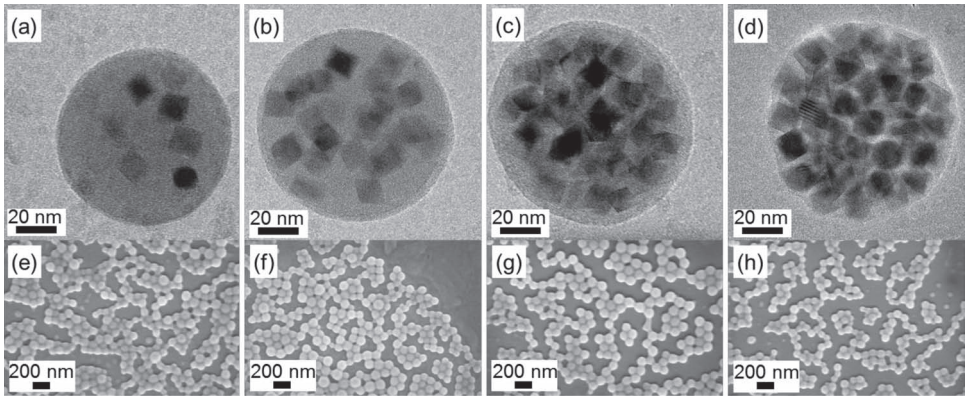

Figure 2. TEM images of a) MFNC-1, b) MFNC-2, c) MFNC-3, and d) MFNC-4. SEM images of e) MFNC-1, f) MFNC-2, g) MFNC-3, and h) MFNC-4.

the metal precursors. The as-synthesized MFNs were completely dispersed in hexane or other non-polar solvents to form a perfect ferrofluid. TEM images in Figure 1a clearly showed that the MFNs were octahedral with a mean size of 18.4 ± 0.9 nm. The particle size was taken as the tip-to-tip long-axis of the octahedron. The particles were highly uniform in morphology and monodisperse in size. The lattice fringes shown in the high-resolution TEM image (Figure 1b) revealed the high crystallinity of these particles and the lattice spacing between two adjacent planes was measured to be 0.481 nm and 0.293 nm, which agreed well with the *d*-spacing of the (111) and (220) lattice planes, respectively, of $MnFe_2O_4$. The selected area electron diffraction (SAED) pattern of the sample (Figure 1c) further proved the formation of $MnFe_2O_4$, with the diffraction peaks for the as-prepared MFNs being characteristic of the jacobsite ($MnFe_2O_4$) phase. XRD and EDS analysis (supporting Information Figure S1) provided further verification for the formation of $MnFe_2O_4$. To form the magnetic nanocomposites, the MFNs were mixed with the amphiphilic copolymer (PBMA-*g*-C12) using a miniemulsion technique to form manganese ferrite nanocomposites (MFNCs) as shown in Figure 1d. The MFNCs were observed to be spherical and with a narrow size distribution. The MFNCs were successfully formed as spherical composites of MFNs and PBMA-*g*-C12, as confirmed by the TEM image in Figure 1e, with the octahedral nanocrystals dispersed and embedded within the nanogel matrix. Finally, the high-resolution TEM (Figure 1f) verified that the particles within the sphere were the earlier MFNs.

By varying the concentration of MFNs in the miniemulsion system, the amounts of MFNs dispersed in the nanogels could be controlled. In total, four MFNC samples were prepared for the experiments: namely MFNC-1, MFNC-2, MFNC-3 and MFNC-4, according to increasing amounts of magnetic loading. **Figure 2**a–d showed the controlled loading of the MFNs in the spherical matrix. The dark contrast of the octahedral MFNs was clearly observed against the lighter contrast of the polymeric matrix. A gradient change in the MFN loading density was observed in the order of increasing loading density, MFNC-1, MFNC-2, MFNC-3, and MFNC-4. The separation distance between the nanocrystals decreased with increasing packing density because the MFNs were spatially dispersed within the spherical matrix. SEM images in Figure 2e–h further showed that monodisperse MFNCs with good size uniformity were obtained. Thus, it was shown that the loading density of the MFNs could be controlled easily by varying a single parameter. More importantly, nanoparticle agglomeration was prevented as the particles were dispersed uniformly throughout the matrix. The spacing between the magnetic nanocrystals was a key characteristic that could be related to effects on the NMR frequency shift of water protons.

The physical characteristics of the particles are summarized in **Table 1**. The different loading densities of the MFNCs were further confirmed by thermogravimetric analysis (TGA). TGA results can be found in the Supporting Information (Figure S2). The Z-average diameter of the MFNs dispersed in chloroform was determined to be 23.0 ± 0.9 nm using DLS. Subsequently, the Z-average diameters of MFNC-1, MFNC-2, MFNC-3, and MFNC-4 dispersed in water were measured to be 175 ± 25 nm, 146 ± 22 nm, 139 ± 20 nm, and 132 ± 20 nm, respectively. It could be observed here that the hydrodynamic size of the MFNCs decreased with increasing loading density. This observation was consistent with results previously with regard to the controlled loading of spherical magnetite nanoparticles.[16] Such a behavior could be explained by water absorption behavior of the nanogel matrix. More experiments on water absorption properties of the MFNCs will be discussed in the later sections.

Table 1. Summary of the physical characteristics of MFNs and MFNCs.

Sample name	MFN loading [wt%][a)]	Z-average diameter [nm][b)]	PDI[b)]	M_s [emu g^{-1}][c)]
MFN	-	23.0 ± 0.9	0.09	62.4 ± 1.6
MFNC-1	5.6 ± 1.6	175 ± 25	0.06	2.6 ± 0.7
MFNC-2	12.5 ± 3.9	146 ± 22	0.05	4.8 ± 1.5
MFNC-3	25.7 ± 1.5	139 ± 20	0.02	18.8 ± 1.1
MFNC-4	42.1 ± 2.4	132 ± 20	0.07	32.5 ± 1.9

[a)]Weight percentage of $MnFe_2O_4$ in the MFNC as determined using thermogravimetric analysis (TGA); [b)]Intensity-weighted size and polydispersity index (PDI) values measured using DLS; [c)]Saturation magnetization (M_s) as measured using VSM.

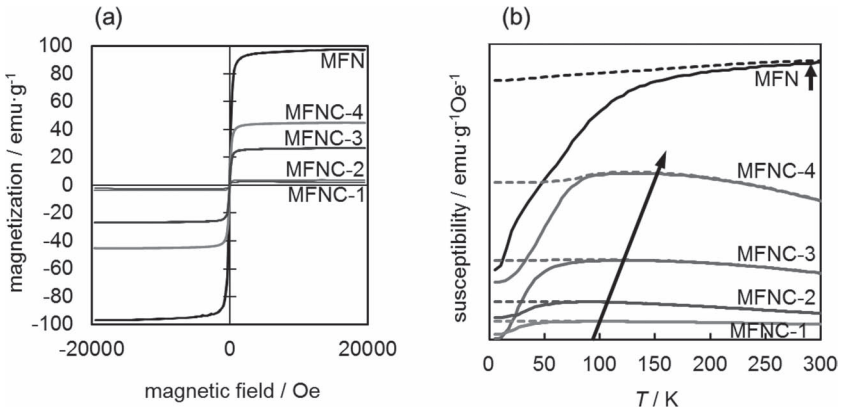

Figure 3. a) $M(H)$ profiles of MFN, MFNC-1, MFNC-2, MFNC-3, and MFNC-4 as measured using VSM. b) ZFC and FC profiles of MFN, MFNC-1, MFNC-2, MFNC-3 and MFNC-4 measured using SQUID. Arrows point to the approximate position of the transition temperature.

2.2. Magnetic Properties

The magnetic properties of the MFNs and MFNCs were evaluated by field-dependent magnetization $M(H)$ measurements at 298 K using a vibrating sample magnetometer (VSM). As shown in **Figure 3**a, the lack of hysteresis loops was characteristic of the superparamagnetic nature of the MFNs and MFNCs. The saturation magnetization (M_s) of the MFNs was found to be 97.1 emu g^{-1}. Subsequently, the MFNCs were found to have M_s values of 2.2 emu g^{-1}, 3.5 emu g^{-1}, 26.5 emu g^{-1} and 44.8 emu g^{-1} for MFNC-1, MFNC-2, MFNC-3 and MFNC-4, respectively. To investigate further, the magnetic properties of MFNC-1, MFNC-2, MFNC-3 and MFNC-4, together with MFNs as a control, were also characterized using a superconducting quantum interference device (SQUID) with the temperature ranging from 5 K to 300 K. In Figure 3b, the temperature-dependent field cooling (FC) and zero-field cooling (ZFC) magnetization curves were recorded. The superparamagnetic-ferromagnetic transition temperature, T_B, was taken as the point of divergence between the FC and ZFC curves, below which the particles were no longer superparamagnetic. From this, the T_B of MFN, MFNC-4, MFNC-3, MFNC-2 and MFNC-1 were determined to be approximately 300 K, 150 K, 130 K, 100 K and 95 K, respectively. The depression of T_B when the MFNs were encapsulated into the polymeric nanospheres to form MFNCs provided evidence that the dipole-dipole interaction between the MFNs was reduced. T_B decreased even more when the loading density of the MFNCs was reduced and tails off at about 95 K which is the approximate blocking temperature T_B of 18 nm $MnFe_2O_4$ particles based on $T_B = KV/25k_B$.[18] The polymer matrix could be seen here as being effective at isolating the magnetic particles, thus reducing the magnetic interactions that lead to the superparamagnetic-ferromagnetic transition.[19] From this, it could be deduced that magnetic particles were distinctly separated and spaced-out within the MFNC nanospheres.

2.3. ^{1}H NMR Study of Magnetic Nanocomposites

In this work, the spectral shift of water protons (^{1}H) by the MFNCs was of interest. The effects of the MFNCs on the NMR signal of water were studied by controlling the concentration of the nanocomposites in solution according to the amount of Fe. Thus, MFNC-2 samples with different Fe concentrations in solution were prepared and the ^{1}H NMR spectra were obtained and placed in overlay in **Figure 4**a. At first, a blank sample containing only pure water was tested to produce a single sharp peak. This main water peak was assigned as 0 ppm for easy referencing. For the 0.05 mM sample, it was observed the occurrence of a secondary peak that was approximately 3.2 ppm upfield from the main water peak. This peak was attributed to the spectral shift of water protons due to the presence of MFNC-2. The integrals of the secondary peaks for the six concentrations of 0.05 mM, 0.5 mM, 1 mM, 2 mM, 3 mM and 4 mM were measured to be 0.03, 0.16, 0.21, 0.11, 0.06 and 0.09, respectively, as compared to their respective main peaks after water suppression. The intensity of the secondary peak appeared to be greatest at the concentration of about 1 mM of Fe. When the concentration was increased further, this secondary peak was observed to broaden. The broadening of the secondary peak was due to the inhomogeneity of the magnetic fields. As we were still unable to ensure that the MNPs were completely homogeneously distributed in the MFNCs, the inhomogeneity might become more pronounced when more MFNCs were present at higher concentrations. Furthermore, as the concentration increased, the internal homogeneity of the magnetic fields might also be affected by external fields of adjacent MFNCs. Thus, the effect of spin-spin interactions (T_2 reduction) became greater which resulted in the broadening of the secondary peak. As a control experiment, the effects of monodisperse MFNs on the ^{1}H NMR spectrum of water were also studied. The MFNs were firstly encapsulated using the same copolymer and same procedure as previously reported to obtain singly dispersed particles in water.[16] Various MFN samples of different Fe concentrations were also prepared. The ^{1}H NMR spectra of these samples were recorded in Figure 4b. In the presence of MFNs, broadening of the main water peak with increased concentration of the MFNs was observed, which was similar to the peak broadening that occurred for the MFNC samples. This behavior is T_2-related and could be better explained in **Scheme 2**. When the magnetic nanoparticles are magnetized, they induce large magnetic field inhomogeniety that leads to a wide range of Larmor precession frequencies of nearby water protons. Hence, the NMR spectrum integrating over these ^{1}H signals covers a wide frequency range, which results in shorter T_2 and a broadened peak. On the other hand, the magnetic field within the MFNC was more uniform, and thus produced a narrower frequency change that could be observed as the secondary peak. Particularly, no obvious secondary spectral peak could be seen with singly-dispersed MFNs. Therefore, this suggests that the secondary peak induced in Figure 4a was caused by the presence of the MFNC structures.

In another experiment, the effects of loading density of the MFNCs on the ^{1}H NMR spectrum of water were studied. As

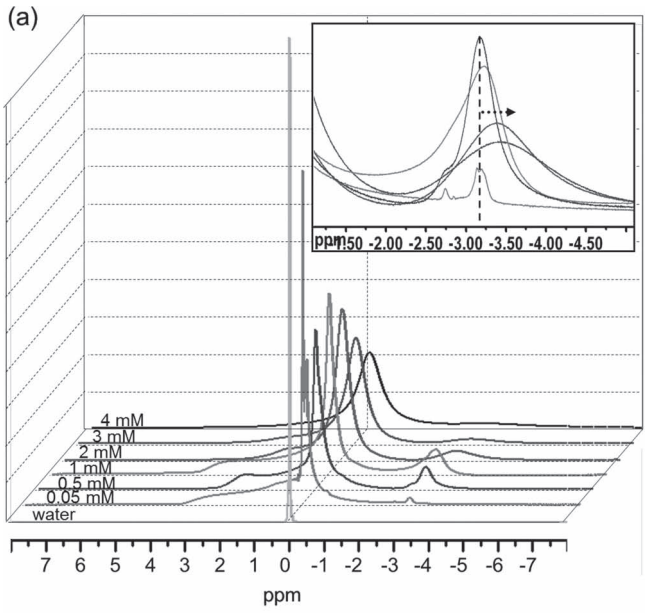

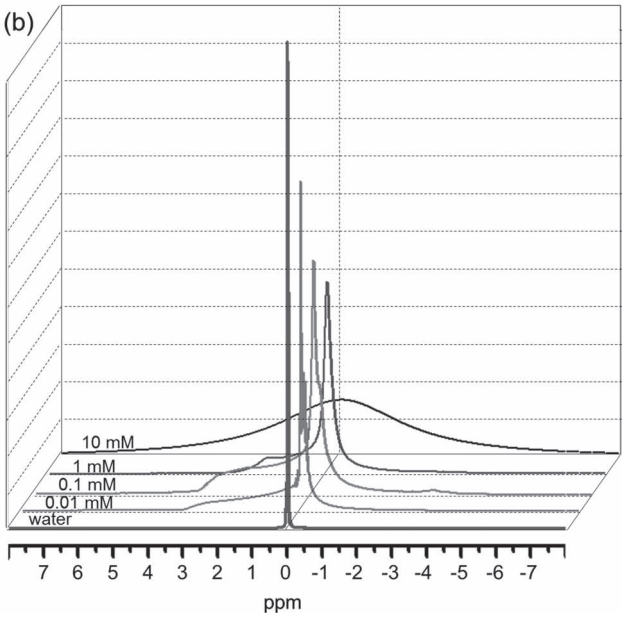

Figure 4. a) ^{1}H NMR spectra of MFNC-2 in water with different Fe concentrations. Inset: Magnified spectra showing the position of the off-resonance peak). b) ^{1}H NMR spectra of MFNs in water with different Fe concentrations.

shown in **Figure 5**, there was no appreciable broadening of the main water peak for the blank nanospheres as compared to pure water. The occurrence of the secondary peak was also absent. For the MFNs, a slight broadening of the main water peak was observed but without the appearance of a secondary peak. The secondary peak was instead observed for all the four MFNC samples. With the concentration of the MFNC samples fixed at 1 mM Fe, a progressive increase in the intensity of the secondary peak at –3.2 ppm from MFNC-4 to MFNC-1 was observed. The area ratios of the secondary peak over the

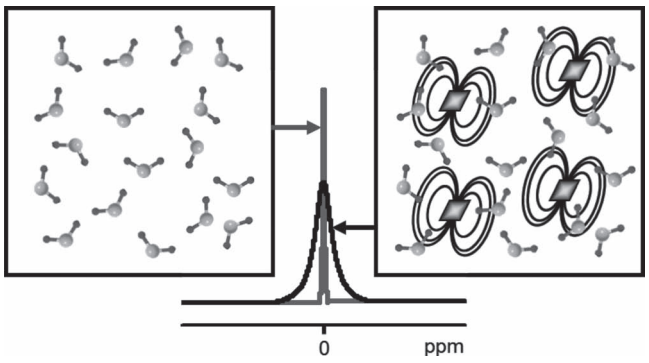

Scheme 2. Broadening effect on the ^{1}H NMR spectrum of water protons due to disturbance of the local magnetic field by magnetic particles.

main water peak after water suppression were calculated to be 0.51, 0.21, 0.05 and 0.02 for MFNC-1, MFNC-2, MFNC-3 and MFNC-4, respectively. Hence, the NMR results have shown that the loading density of the MFNCs had a great effect on the intensity of the secondary peak, and that MFNCs with lower loading induced the most intense peak. This observation suggested that the water within the nanospheres had caused the secondary peak. The nanogel exhibited a certain degree of water absorption capability and water could pass through the nanogels. Thus, the water molecules within the spheres were strongly affected by the inner-field influence of the magnetic cores.

In order to further prove that the secondary peak was caused by the water within the nanospheres, the T_1 and T_2 values at the

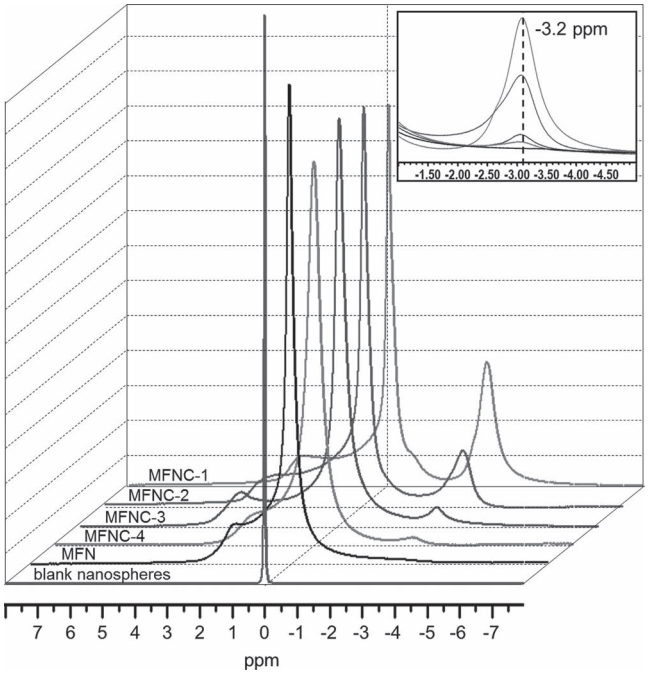

Figure 5. ^{1}H NMR spectra overlay of blank nanospheres, MFNs, MFNC-1, MFNC-2, MFNC-3 and MFNC-4. Inset: Magnified spectra showing the position of the off-resonance peak. Concentrations of samples were fixed at 1 mM Fe.

main (0 ppm) and secondary (–3.2 ppm) peaks for the samples of MFNC-1, MFNC-2, MFNC-3 and MFNC-4 were measured. The Fe concentrations of the four samples were fixed at 1 mM and the relaxivity results are recorded in Table S1 (Supporting Information). In general, the main peak had $T_1 \approx 2000$ ms and $T_2 > 15$ ms. In comparison, the relaxation times of the secondary peak were very short, i.e., $T_1 \approx 270$ ms and $T_2 \approx 6$ ms. T_1 and T_2 at the secondary peak did not change much with different loading density. The very short T_1 and T_2 values of the secondary peak suggest very strong relaxation effects. This implied that the protons were in close proximity to the manganese ferrite particles. If the secondary peak was due to protons external of the MFNC spheres, then the T_1 should have been much longer, because the contribution due to spin-lattice effect would be insignificant. Hence, this could be used as evidence that the off-resonance peak was mainly due to water within the MFNC spheres.

However, it was observed that the peak shift was not a function of loading. This could be attributed to the limited variation in separation distance between MFNs within the nanospheres. As shown in Figure 1, the as-obtained nanospheres were quite small (≈100 nm under TEM). The separation distance variation within the spheres was quite limited, thus it was difficult to produce a substantial change in the localized magnetic field by changing loading. Therefore, the peak shift with change in loading was quite small. Furthermore, as mentioned early, the distribution of MNPs in the nanospheres was not completely uniform, which made the secondary peak relatively broad, and thus it was difficult to detect the peak shift.

2.4. MR Spectroscopic Imaging Study

Phantoms composed of several tubes of MFNCs was prepared and scanned at 9.4T MRI. Offset frequency was determined experimentally and the phantom images of MFNCs were acquired at frequency offsets of +2000 Hz, 0 Hz, and –2000 Hz. **Figure 6** showed the MR spectroscopic images of MFNC-1, MFNC-2 and MFNC-3 solutions at the different frequency offsets. At 0 Hz offset, it could be observed the T_2 shortening

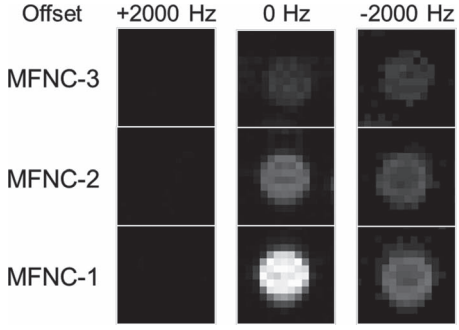

Figure 6. MR spectroscopy images MFNC-1, MFNC-2 and MFNC-3 (1 mM Fe) dispersed in water. T_2^*-weighted images were acquired by applying a gradient echo sequence (T_R = 20 ms; T_E = 4 ms; flip angle = 20°). The phantom samples were excited by RF pulses for 5 ms at a frequency offsets of 0 Hz and ±2000 Hz from bulk water. The chemical shift image was acquired with spin-echo sequence (T_R = 2 s; T_E = 6.5 ms).

properties of the MFNCs. The r_2 molar relaxivities of MFNC-1, MFNC-2, MFNC-3 and MFNC-4 were determined to be 191.9, 226.4, 427.4 and 632.59 $s^{-1}mM^{-1}$ Fe, respectively. Hence, the MFNCs induced darker contrasts with increased darkening from MFNC-1, MFNC-2 to MFNC-3. These results were consistent with our previous work, in which the increasing loading density resulted in greater T_2 relaxivity.[16] At –2000 Hz offset, the MFNCs showed positive contrast with increased intensity from MFNC-3, MFNC-2 to MFNC-1. These results agreed well with the NMR spectra in Figure 5, where there was an increasing peak intensity of the secondary peak at –3.2 ppm towards the lower loading MFNCs. A comparison with the scan at +2000 Hz revealed that there was no signal induced by the MFNCs. Therefore, it was concluded that the positive contrast generated at –2000 Hz offset was caused by the frequency shift of water protons by the MFNCs.

Overall, the results suggested a spectral shift of water protons caused by the MFNCs, which was resultant from a combined effect between the MFN and the nanogel matrix. It was strongly believed that water molecules within the MFNCs were responsible for the observation of this phenomenon. To prove that there was actual substantial water penetration into the MFNC nanospheres, the following water absorption tests were conducted.

2.5. Water Swelling Study

The water swelling properties of the MFNCs were compared against the nanoparticles encapsulated in poly(styrene)-*b*-poly(methyl methacrylate) (PS) spheres. The latter samples were prepared using the exact same method as the MFNCs except that the polymer encapsulant was changed to PS, which was chosen because of its strong hydrophobic properties and was expected to exhibit minimal swelling properties. The nanocomposites encapsulated in PS were labeled as MFNC-PS. MFNC-PS-1 had similar loading density as MFNC-2 (10.3 ± 2.6 wt%), while MFNC-PS-2 had similar loading density as MFNC-3 (27.0 ± 1.2 wt%). Firstly, the average sizes of the nanospheres in dry state were measured for each sample under the SEM, using a sample size of 100 particles each. Then the hydrodynamic radius of each sample dispersed in water was measured using DLS. **Figure 7**a summarized the results of the size measurements. By comparing the difference between the dry state and hydrodynamic size, the percentage size difference could be derived. Depending on the loading density, the MFNC samples showed a 30% to 65% size change. On the other hand, the MFNC-PS samples showed only about 7% to 10% size difference between the dry state and the hydrodynamic size. Hence, these results explicitly showed that the MFNCs had a more significant increase in size than the MFNC-PS when dispersed in water. This provided the first evidence for volumetric swelling of the nanospheres due to water absorption.

2.6. Water Permeability Tests

In another test, silver nanoparticles were encapsulated into the polymeric nanospheres instead of MFNs. Ag nanoparticles are

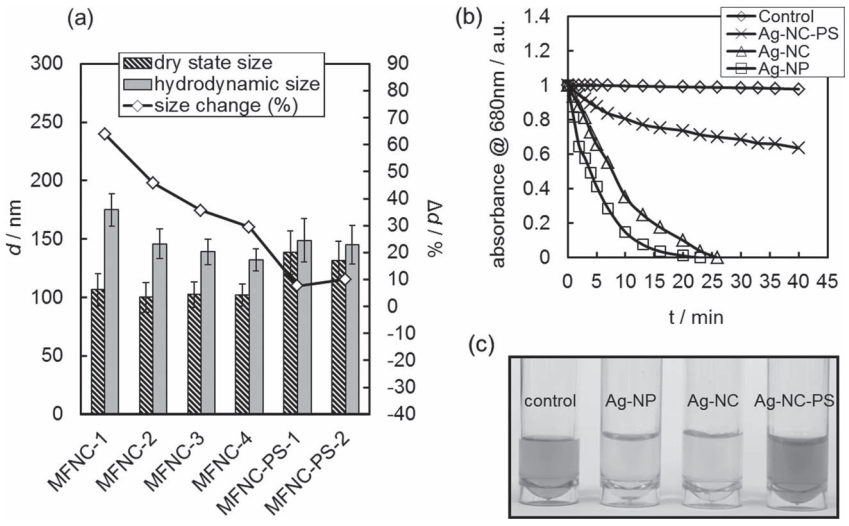

Figure 7. a) Left axis: Comparison of the sizes of the respective nanospheres in dry state to the hydrodynamic size in solution as measured using DLS. Right axis: Percentage size difference between dry state and hydrodynamic size of the samples. b) Absorbance profiles of a blank control sample, Ag-NP, Ag-NC and Ag-NC-PS at λ_{max} = 680 nm with respect to time. c) Digital photographs under normal light illustrating the decolourization of methylene blue in aqueous $NaBH_4$ (control) and in the presence of Ag-NP, Ag-NC, and Ag-NC-PS. Photographs were taken 40 min after addition of particles.

known to be an effective catalyst for the reduction of methylene blue in a reducing environment. However, its catalytic efficiency is dependent on its availability to interact with the chemicals. Hence, the ability of water and small molecules to permeate the encapsulating matrix could be examined with respect to the type of polymer used. Through such observations, the relative permeability of the polymeric matrix could be studied. Thus, an aqueous solution containing methylene blue and the reducing agent sodium borohydride ($NaBH_4$) was used to demonstrate the catalytic effect of the Ag nanoparticles encapsulated with different materials. The synthesis of Ag nanoparticles can be found in Figure S3 (Supporting Information). Ag nanoparticles were either encapsulated into PBMA-*g*-C12 (Ag-NC) or encapsulated into poly(styrene)-*b*-poly(methyl methacrylate) (Ag-NC-PS). A sample consisting of phase transferred monodisperse silver nanoparticles (Ag-NPs) was also prepared for comparison. The experiment for assessing the catalytic efficiency of Ag follows closely a protocol previously reported.[20] The test was performed by mixing methylene blue/$NaBH_4$ solution with the respective Ag samples. The absorbance spectra (Figure 7b) were obtained by measuring the absorbance at 680 nm at pre-determined time intervals after addition of the samples. Reduction of methylene blue was characterized by the amount of absorbance at 680 nm. Results showed that the control (without addition of catalyst) did not undergo significant reduction over the period of 40 min. However, for the samples Ag-NP, Ag-NC, Ag-NC-PS, the rate of decolouration was accelerated substantially. The decolouration for Ag-NP and Ag-NC was also observed to occur significantly faster than for Ag-NC-PS. Figure 7c showed the colour of the methylene blue solutions after 40 min incubation with the three samples. The blue coloration of methylene blue had completely disappeared after catalytic reduction by Ag-NP and Ag-NC. However, the blue coloration was only partially reduced by Ag-NC-PS, which finally appeared green due to combined light absorbance by Ag at the shorter visible wavelength (blue) and absorbance by methylene blue at the longer visible wavelengths (red). The rate of reduction of methylene blue was in the order Ag-NP > Ag-NC > Ag-NC-PS. Hence, it was demonstrated that the type of polymer coating had a significant effect on the catalytic efficiency. This demonstrated the ability of water and small molecules such as methylene blue to penetrate the interior of the PBMA-*g*-C12 nanospheres.

In order to further quantify the amount of water absorbed by the nanospheres, we measured the water absorption of a 50 mg PBMA-*g*-C12 pellet. The results can be found in Table S2 of the Supporting Information. Up to 42.3 wt% water was absorbed after 7 days. This result showed that the polymer material was able to absorb a substantial amount of water. We calculated the vol% of MFNC spheres in water for 1 mM [Fe] samples using TGA data and assuming the density of $MnFe_2O_4$ and polymer matrix to be 5.15 and 1.3 g cm^{-3}, respectively. By taking a conservative 40% of water absorbed in each MFNC, the total water in the spheres could be estimated. These were compared to the ^{1}H NMR peak ratios. The NMR peak ratios here were obtained without water suppression for comparison. The results are presented in Table S3 (Supporting Information). Calculations also showed that NMR peak ratios correspond well to the estimated amount of water in the spheres.

2.7. Tuning of Hydrophilicity by PEG Conjugation

The last two tests showed that it was possible for a substantial degree of water permeability in the MFNC nanospheres. To further improve the water penetration capability of the MFNCs, the brush copolymer (PMBA-*g*-C12) was conjugated with poly(ethylene glycol) (PEG; MW = 2000 Da) to improve its hydrophilicity. **Figure 8** showed the TEM image of a typical nanocluster formed using PBMA-*g*-(C12/PEG). In this sample, approximately 25% of the maleic anhydride of PBMA was grafted with PEG. ^{1}H NMR measurements of MFNC-2, MFNC-PS-1 and MFNC-PEG (all 3 samples having approximately the same nanoparticle loading of 10 wt%) were collated for comparison. The main water peak was normalized and the results showed a marked increase in the intensity of the secondary peak at −3.2 ppm after conjugation with PEG. It proved that the intensity of the secondary peak was dependent on the water density within the MFNCs. On the other hand, MFNC-PS exhibited a lowered intensity for the secondary peak. Hence, it could be concluded that the MFNC allowed a good degree of water penetration and that water molecules trapped within the spheres were the most probable cause of the appearance of the secondary peak.

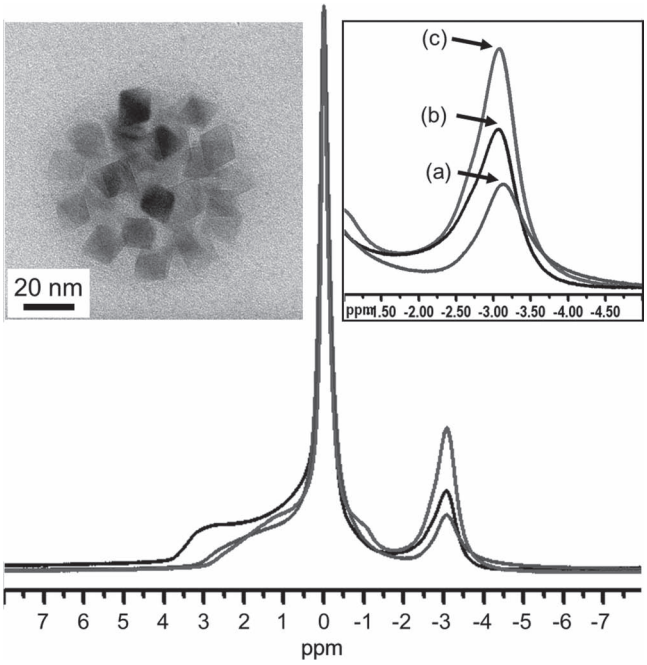

Figure 8. ^{1}H NMR spectra of MFNC-PS, MFNC-2 and MFNC-PEG in water. Inset (right): a) MFNC-PS-1, b) MFNC-2, and c) MFNC-PEG. Inset (left): TEM image of a MFNC-PEG composite nanosphere.

2.8. pH Stability

For biomedical applications, it was necessary to ensure that the MFNCs remain a stable dispersion in various buffer mediums and in blood serum. The MFNCs should firstly be completely dispersed in water or phosphate buffered saline (PBS). From our experiments, the MFNCs were observed to remain stable in water or PBS for weeks. To investigate the effects of pH on the colloidal stability of the MFNCs, the particles were treated in solutions of different pH ranging from 1 to 13, as shown in **Figure 9**a. MFNC-4 was used for this part of the experiments because it contained the highest Fe content. For the first day, it was observed that between pH 1–pH 11, the size of MFNC-4 remained relatively constant within the range of 128–136 nm. However, at pH 13 the size decreased drastically within seconds to 40 nm upon dispersing the particles in the alkaline media. If we compare this to the singly-dispersed MFNs (35 nm in water), it could be deduced that the nanocomposite spheres had disintegrated to become individual nanoparticles at pH 13. This was due to the hydrolysis and dissolution of the excess polymer matrix, leaving only those polymer chains that were directly bound on the nanoparticles surfaces to remain stable. After 7 days, the MFNCs dispersed in mediums from pH 3 to pH 11 and PBS remained stable in size. However, MFNCs in the more extreme pH conditions did not exhibit similar stability. This was not unexpected because the MFNCs in pH 1 medium were subjected to intense protonation of the carboxylate groups and dissolution of the ferrite cores. As a result, the MFNCs in pH 1 medium exhibited signs of agglomeration as time passed. The sample in pH 13 medium was also unstable although it became a dispersion of stable nanoparticles (34 nm) after only 1 day. Figure 9b showed the iron dissolution study of MFNCs after the 7 day incubation period. The amounts of Fe^{3+} ions liberated from the MFNCs were determined after the 7 days using ICP analysis. Minimal leaching of iron from the MNFCs was observed for pH 5 to pH 13, with iron release being much higher at pH 3 and pH 1. This implied that the ferrite cores of the MFNCs were generally stable against corrosion at pH levels in the range of 5–13. Hence, it could be concluded that the MFNCs were stable over a wide range of pH from 5–11, which was sufficient for application in typical physiological conditions.

2.9. Colloidal Stability

The long-term colloidal stability of the MFNCs in the presence of serum protein was also investigated. The MFNCs

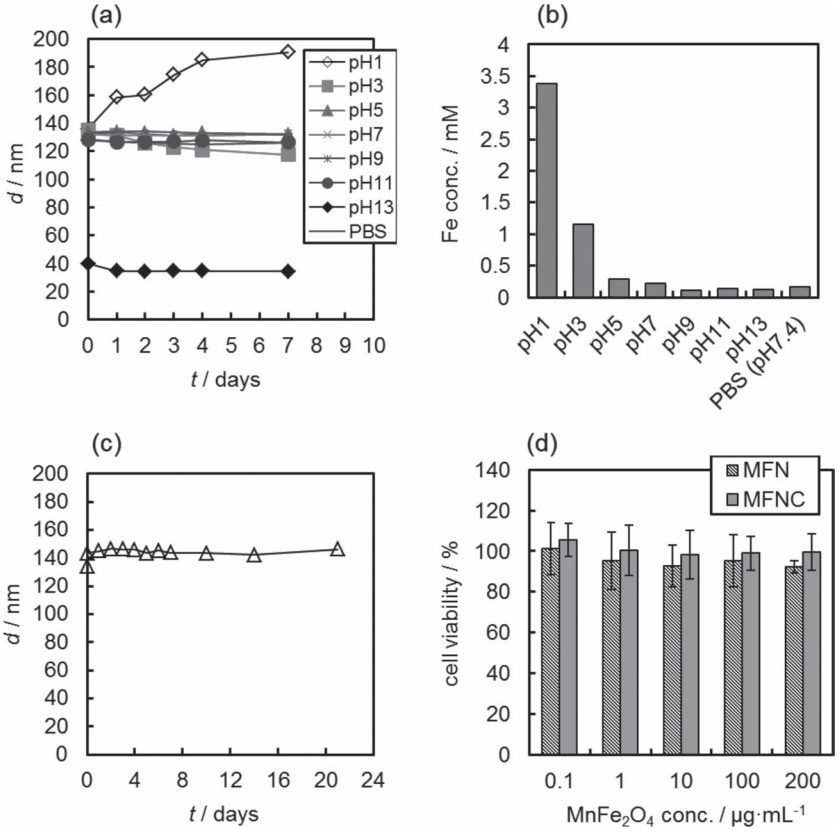

Figure 9. a) Size evolution of MFNC-4 in different pH media for 7 days. b) Amount of Fe^{3+} liberated from MFNC-4 after incubated in different pH media for 7 days at 37 °C. c) Size evolution of MFNC-4 dispersed in PBS containing BCS (10%) at 37 °C for 21 days. d) Cell viability of NIH/3T3 cell lines incubated with different concentrations of MFN and MFNC-4.

were dispersed in PBS containing 10% BCS (bovine calf serum) and incubated at 37 °C for up to 21 days. The size was monitored real-time using DLS and recorded in Figure 9c. Apart from the initial increase in particle size from 134 nm to 144 nm (≈7.5% increase), the particles neither exhibited a meaningful increase in size nor decrease in derived count rate. Therefore, it was shown that MFNC-4 was stable in the presence of serum proteins for extended periods of time. The high colloidal stability of the nanoparticles could be attributed mainly to the biocompatible PVA coating that was physisorbed onto the surface of the particles during the miniemulsion process. Thus, it was experimentally shown that the MFNCs exhibited high colloidal stability and was suitable for application in vivo.

2.10. Cell Viability Tests

Cytotoxicity of the nanoparticles is another important issue for application in biological experiments. Therefore, NIH/3T3 cells were incubated with MFN or MFNC-4 at different concentrations and its viability was evaluated using CCK-8 assay. Figure 9d shows that there was no significant decrease in the viability of the NIH/3T3 cells within the particle concentration range from 0.1–200 μg mL^{-1}. 200 μg mL^{-1} of MFNCs corresponds to about 1.5 mM of Fe in the sample, which was close to the optimum concentration for inducing the highest intensity for the secondary peak in the NMR experiments. Hence, the MFNCs were shown to exhibit suitable biocompatibility for the required operational concentrations. Coupled with its relatively good pH stability, it was concluded that the MFNCs were safe for administration into the body for concentrations of 200 μg mL^{-1} or less.

3. Conclusions

Manganese ferrite nanocomposites (MFNCs) were synthesized by controlling the loading of manganese ferrite nanoparticles in polymeric nanospheres. The MFNCs could be highly magnetized in a magnetic field and caused a frequency shift for water protons as shown in NMR experiments. This effect was investigated and the main cause was attributed to the water absorption capability of the nanospheres. The chemical shift of water was –3.2 ppm, which could be exploited for specific detection of contrast agent using MR spectroscopic imaging. By performing the MR imaging at an offset frequency from the main water peak, the background interference by water could be effectively eliminated. Hence, only the regions affected by the MFNCs would be detectable. Furthermore, the MFNCs were shown to exhibit excellent colloidal stability as well as pH stability in the pH range of 5–11. Therefore, the MFNCs are potentially useful for T_2-weighted and MR spectroscopy dual imaging for more effective differentiation of targeted organs and tissues.

4. Experimental Section

Materials: Poly(isobutylene-*alt*-maleic anhydride) (PBMA; $M_w \approx 6000$, 85%), 1-dodecylamine (98%), and poly(vinyl alcohol) (PVA; average M_w 31 000–50 000, 87–89% hydrolyzed) were obtained from Aldrich. Iron(III) acetylacetonate ($Fe(acac)_3$; 97%), manganese(II) acetylacetonate ($Mn(acac)_2$; 97%), and oleic acid were purchased from Fluka. Benzyl ether (99%) and tetrahydrofuran (THF; 99.9%) were purchased from Aldrich. Hexane (J.T. Baker, 99.0%) and chloroform (Fisher Scientific; 99.99%) were used as received. Cell Counting Kit-8 (CCK-8) was purchased from Dojindo Molecular Technologies, Inc.

Measurements: Scanning electron microscopy (SEM) was performed using a XL 30 FEG Philips, Hillsboro, OR. Transmission electron microscopy (TEM) was performed using a JEOL 100CX electron microscope with an acceleration voltage of 200 kV. X-ray diffraction (XRD) patterns were recorded on a powder diffractometer (D8 Advanced Diffractometer System, Bruker, Karlsruhe, Germany) with Cu K_α (1.5418 Å) radiation at room temperature. Thermogravimetric analysis (TGA) was performed using an SDTQ600 instrument. Inductively coupled plasma (ICP) analysis was performed using a PerkinElmer Dualview Optima 5300 DV ICP-OES system. Magnetic properties were characterized by vibrating sample magnetometry (VSM) at room temperature, and superconducting quantum interference device (SQUID) magnetometer at temperatures ranging from 5 to 300 K. The hydrodynamic diameters of samples were obtained by dynamic light scattering (DLS) measurements using a Malvern Zetasizer Nano-ZS equipped with a 633 nm He-Ne laser was used as the light source.

Synthesis of Amphiphilic PBMA-g-C12 Brush Copolymer: The synthesis of the amphiphilic copolymer, poly(isobutylene-*alt*-maleic anhydride) (PBMA) grafted with 1-dodecylamine (C12), followed closely to previously reported procedures.[21] In a cap sealed conical flask, PBMA (1 g, 6.5 mmol anhydride) and 1-dodecylamine (0.9 g, 75 mol% anhydride) were mixed into THF (15 mL), wherein PBMA was initially insoluble. The reaction flask was then heated to 50 °C and a reaction was observable by the solubilization of PBMA to form a clear solution. The reaction mixture was incubated overnight to ensure complete reaction. Finally, the product, PBMA-*g*-C12, was extracted by solvent evaporation and then dried in vacuo at room temperature for 2 days to obtain an off-white powder.

Synthesis of PBMA-g-(C12/PEG) Brush Copolymer: The synthesis of PBMA-*g*-(C12/PEG) involved a two-step process. The first step was an acid-catalyzed reaction between PBMA and mPEG, according to a previously report method.[22] To obtain approximately 25% conversion of anhydride rings, PBMA (1 g, 6.5 mmol anhydride) and mPEG (3.25 g, 1.6 mmol) was mixed in THF (45 mL) and heated at 65 °C in a conical flask equipped with a condenser column. Fuming HCl (10 M, ≈25 drops) was added to the mixture and then the reaction flask was left to stir under reflux. The reaction was observable after several hours of heating with the solubilization of PBMA to form a clear solution. The reaction was left to continue for 12 h to ensure complete reaction. After the reaction was stopped, the solution was neutralized using sodium hydroxide solution (1 M) and the copolymer was precipitated using cold anhydrous diethyl ether. The product, PBMA-*g*-PEG, was extracted by centrifugation and then dried in vacuo for 2 days. The second step involved the grafting of 1-dodecylamine to the PBMA-*g*-PEG following the procedure in the previous section to obtain PBMA-*g*-(C12/PEG) composed of 75 mol% C12 and 25 mol% PEG.

Synthesis of Octahedron 18 nm Oleic Acid-Capped $MnFe_2O_4$ Nanoparticles: The synthesis of $MnFe_2O_4$ nanoparticles (MFNPs) followed closely the procedures as reported in this article by Li et al. with slight modification.[23] Monodisperse $MnFe_2O_4$ nanoparticles (average particle diameter: 18 nm) were synthesized in a one-pot reaction using the basic formulation: $Fe(acac)_3$ (8 mmol), Mn(acac)2 (4 mmol), oleic acid (28 mmol), and benzyl ether (35 mL) were charged into a three-neck round bottom flask. The temperature was slowly raised from room temperature to 165 °C and maintained isothermally for 30 min. The reaction flask was then quickly heated to 280 °C. Finally, the reaction mixture was refluxed at 280 °C for 30 min to allow the nanocrystals to grow. The resulting black mixture was cooled and washed by repeated dispersion and precipitation using hexane and ethanol, respectively. Larger particles were ferromagnetic and could be removed by magnetic separation. The final product was dispersed completely in chloroform

(50 mg mL^{-1}) and the resultant ferrofluid was stored in a sealed glass vial.

Formation of Manganese Ferrite Nanocomposites: The formation of MFNCs was achieved by the combination of miniemulsion and solvent evaporation techniques as described in a previous work.[16] Firstly, PBMA-*g*-C12 and MFNs were dissolved completely in chloroform. Variable amounts of MFNs were used to achieve different nanocluster loading densities according to Table 1. The chloroform solution was then emulsified with 10× volume excess of water (1 wt% PVA as stabilizer) using a homogenizer (SONICS VCX 130 PB) at 20 kHz frequency and 60% amplitude for 5 min. The emulsion was then warmed at 50 °C in an open glass beaker under rapid stirring to allow the chloroform to evaporate. The as-prepared MNFCs formed a clear colloidal solution of magnetic nanocomposites in water. The colloid firstly underwent centrifugation at 2000 rpm for 10 min to remove unusually large aggregates. The colloid was then purified by centrifugation at 8000 rpm for 10 min to extract the MNFCs, which were then re-dispersed in water/methanol (50:50). The purification process was repeated at least twice before the MNFCs were finally dispersed in water or appropriate aqueous medium.

Colloidal Stability of the MFNCs: The colloidal stability of the as-prepared MFNCs was investigated by dispersing it in various aqueous media, namely de-ionized water, PBS solution, hydrochloric acid solutions (pH 1, 3 and 5), and aqueous sodium hydroxide (pH 9, 11 and 13). The MFNCs were also incubated in PBS (with 10% BCS) at 37 °C to study the interaction with proteins in a serum. For these experiments, MFNC-4 was chosen for study. Typically, MFNC-4 (50 μg mL^{-1} in 0.1 mL of water) was mixed with the respective pH solutions (0.9 mL). After predetermined time intervals, the stability of the MFNC solutions was evaluated by particle size measurements using DLS.

CCK-8 Cytotoxicity Assay: NIH/3T3 cells were seeded into a 96-well plate at 7500 cells per well and were incubated for 12 h at 37 °C, 5% CO_2 in air. The growth medium was removed before the NIH/3T3 cells were treated with MFNs or MFNCs in DMEM (Dulbecco's modified Eagle medium) supplemented with 10% BCS at different particle concentrations. The cell lines were incubated with the particles for 24 h. Then CCK-8 solution (10 μL) was added to each well and shaken slightly to mix well. After a further incubation time of 3 h, the plate was analyzed using a microplate reader by measuring the absorbance at 450 nm.

^{1}H Chemical Shift of Water by MFNCs: ^{1}H NMR experiments were performed on our Bruker AV500 NMR spectrometer (500 MHz) equipped with BBO probe. Measurements were done in pure water (H_2O), so pure deuterium oxide was used to tune and match the probe, and pre-shim the magnet before measurement of the magnetic samples. The NMR spectrum was obtained by suppressing the main water peak by pre-saturation at the on-resonance frequency of the main water peak.

MRI Test: MRI experiments were conducted in a 9.4 Tesla MRI scanner (Varian, Agilent Inc, USA) using a birdcage coil at room temperature. The MRI phantom samples were prepared by drawing the MFNC solutions into 1 mL disposable poly(propylene) syringes. The concentration of each sample was 1 mM Fe. Off-resonance experiments were carried out using a 2D gradient echo and chemical shift imaging pulse sequence with a frequency-selective sine-shaped pulse. The T_2^*-weighted image was acquired using a gradient echo sequence (T_R = 20 ms; T_E = 4 ms; flip angle = 20°). The phantom samples were excited by RF pulses for 5 ms at a frequency offsets of 0 Hz and ±2000 Hz from bulk water. The chemical shift image was acquired with spin-echo of spectral width of 5000 Hz (T_R = 2 s; T_E = 6.5 ms).

Supporting Information

Supporting Information is available from the Wiley Online Library or from the author.

Acknowledgements

The authors would like to thank the financial support provided by Singapore MOE Tier 1 grant R-284-000-088-112. They would like to thank Dr. Guilhem Pages and Dr. Qiong Ye from Singapore Bioimaging Consortium for the help with the NMR measurements.

Received: January 30, 2012
Revised: August 7, 2012
Published online: September 4, 2012

[1] A. M. Blamire, *Br. J. Radiol.* **2008**, *81*, 601.
[2] J. C. Richardson, R. W. Bowtell, K. Mader, C. D. Melia, *Adv. Drug Delivery Rev.* **2005**, *57*, 1191.
[3] E. Terreno, D. D. Castelli, A. Viale, S. Aime, *Chem. Rev.* **2010**, *110*, 3019.
[4] F. Q Hu, H. M. Joshi, V. P. Dravid, T. J. Meade, *Nanoscale* **2010**, *2*, 1884.
[5] P. Caravan, J. J. Ellison, T. J. McMurry, R. B. Lauffer, *Chem. Rev.* **1999**, *99*, 2293.
[6] A. Senpan, S. D. Caruthers, I. Rhee, N. A. Mauro, D. Pan, G. Hu, M. J. Scott, R. W. Fuhrhop, P. J. Gaffney, S. A. Wickline, G. M. Lanza, *ACS Nano* **2009**, *3*, 3917.
[7] D. D. Stark, R. Weissleder, G. Elizondo, P. F. Hahn, S. Saini, L. E. Todd, J. Wittenberg, J. T. Ferrucci, *Radiology* **1988**, *168*, 297.
[8] R. Weissleder, P. F. Hahn, D. D. Stark, G. Elizondo, S. Saini, L. E. Todd, J. Wittenberg, J. T. Ferrucci, *Radiology* **1988**, *169*, 399.
[9] S. Viswanathan, Z. Kovacs, K. N. Green, S. J. Ratnakar, A. D. Sherry, *Chem. Rev.* **2010**, *110*, 2960.
[10] K. M. Ward, A. H. Aletras, R. S. Balaban, *J. Magn. Reson.* **2000**, *143*, 79.
[11] K. Glunde, D. Artemov, M. F. Penet, M. A. Jacobs, Z. M. Bhujwalla, *Chem. Rev.* **2010**, *110*, 3043.
[12] Z. X. Jiang, Y. Feng, Y. B. Yu, *Chem. Commun.* **2011**, *47*, 7233.
[13] G. Zabow, S. J. Dodd, J. Moreland, A. P. Koretsky, *Nature* **2008**, *453*, 1058.
[14] G. Zabow, S. J. Dodd, J. Moreland, A. P. Koretsky, *Nanotechnology* **2009**, *20*, 385301.
[15] J. S. Ananta, B. Godin, R. Sethi, L. Moriggi, X. W. Liu, R. E. Serda, R. Krishnamurthy, R. Muthupillai, R. D. Bolskar, L. Helm, M. Ferrari, L. J. Wilson, P. Decuzzi, *Nat. Nanotechnol.* **2010**, *5*, 815.
[16] E. S. G. Choo, X. S. Tang, Y. Sheng, B. Shuter, J. M. Xue, *J. Mater. Chem.* **2011**, *21*, 2310.
[17] O. C. Andronesi, D. Mintzopoulos, N. Psychogios, M. Kesarwani, J. X. He, S. Yasuhara, G. Dai, L. G. Rahme, A. A. Tzika, *Magn. Reson. Imaging* **2010**, *32*, 1172.
[18] S. Yoon, K. M. Krishnan, *J. Appl. Phys.* **2011**, *109*, 07B534.
[19] D. Caruntu, G. Caruntu, C. J. O'Connor, *J. Phys. D: Appl. Phys.* **2007**, *40*, 5801.
[20] L. Li, E. S. G. Choo, X. S. Tang, J. Ding, J. M. Xue, *Acta Mater.* **2010**, *58*, 3825.
[21] C. A. J. Lin, R. A. Sperling, J. K. Li, T. Y. Yang, P. Y. Li, M. Zanella, W. H. Chang, W. J. Parak, *Small* **2008**, *3*, 334.
[22] W. W. Yu, E. Chang, J. C. Falkner, J. Y. Zhang, A. M. Al-Somali, C. M. Sayes, J. Johns, R. Drezek, V. L. Colvin, *J. Am. Chem. Soc.* **2007**, *129*, 2871.
[23] L. Li, Y. Yang, J. Ding, J. M. Xue, *Chem. Mater.* **2010**, *22*, 3183.